Enhanced out-of-plane piezoelectricity of group-III(A) Janus hydrofluoride monolayers

He-Na Zhang ⬤, Yang Wu, Chunhua Yang, Liang-Hui Zhu, and Xiao-Chun Wang ⬤[*]
Institute of Atomic and Molecular Physics, Jilin University, Changchun 130012, China

Two-dimensional (2D) piezoelectric materials utilizing the unique electronic characteristic were widely needed for microelectronic sensors and energy conversion devices. However, the currently reported 2D piezoelectric films face thorny challenges in practical application due to lack of the mechanical durability or the strong vertical piezoelectric effect. Herein, based on first-principles calculations, we theoretically simulate the Janus semiconductor nanosheets, namely, F-M-H (M = B, Al, and Ga) monolayers. The result shows that they have admirable dynamical and thermal stabilities to achieve strong mechanical durability and possess the desired vertical piezoelectric effect by applying uniaxial strain in the z-axis direction vertical to the nanosheet surface. For the three materials, F-B-H has the strongest stability and the most significant vertical piezoelectric effect. The out-of-plane piezoelectric stress coefficient e_{31} of F-B-H is higher than other reported 2D piezoelectric SnOSe films by two orders of magnitude. Furthermore, we found an interesting relationship among these three nanosheets: the higher the electronegativity difference ratio, the higher the piezoelectric stress coefficient. Finally, this work not only deepens the understanding of 2D piezoelectric materials, but also provides a platform for fabricating cutting-edge piezoelectric equipment such as wearable electronic, medical blood pressure detectors and robotic bionic skin tactile sensors.

I. INTRODUCTION

Two-dimensional (2D) materials possess a series of unique electric, optics, and mechanics properties [1–3], for example, the on-site proton transfer phenomenon in the magnetic switch [4] and the electron reservoir performance in methane conversion [5], and 2D piezoelectric materials can achieve the energy transformation between mechanical and electrical energy by using unique characteristics [6,7]. Recently, 2D piezoelectric nanostructure materials have been used as sensors, energy harvesters, and actuators [8,9]. Like the transition metal dichalcogenide MoS_2, the monolayer of hexagonal boron nitride (h-BN), the group II(A) and II(B) metal oxides, and the hexagonal group III-V(A) semiconductors are all familiar piezoelectric crystals [10–15]. However, the practical applications of piezoelectric materials have remained challenges, such as the low vertical piezoelectric effect and weak mechanical durability. Especially, robotic tactile sensors and blood pressure detectors both play an important role in their respective fields. These applications require the nanomaterials with specific piezoelectrics by applying uniaxial strain along the z-axis direction vertical to the nanosheet. Hence, it is of great significance to find a stable 2D piezoelectric material with a highly effective vertical piezoelectric effect, in order to improve the accuracy and efficiency of these cutting-edge devices.

Both boron and carbon atoms have sp^2 hybrid orbitals. So, boron atoms can form a graphene-like (borophene) structure. Borophene is a special 2D material due to high Fermi velocity, light transmittance, electron mobility, and stable band gap structure [16–20]. However, research results show that borophene is unstable in the air [21]. Generally, surface modification and adsorption are applied to solve this problem, for example, borohydride. At the same time, surface modification is one of the ways to realize piezoelectricity. Du *et al.* predicted four dynamically stable 2D borohydride structures (with space group $C2/m$, $Pbcm$, $Cmmm$, and $Pmmn$) [22,23]. Distinctively, the honeycomb nanostructure of $Cmmm$ (B_4H_4) contains twisted Dirac cones with ultrahigh Fermi velocity in the Brillouin zone and has a very flexible band adjustability [24–28]. As is well known, the piezoelectric materials need to have a nonzero electronic band gap and a noninverse symmetry. B_4H_4 has a unique band gap and a decent structural symmetry. The conversion of nonpiezoelectric material to piezoelectric material can be achieved by breaking the Dirac cone near the Fermi level and the symmetry of the structure. The elements on both sides of the B atom layer are the same kinds. If the elements are replaced by different atoms, the symmetry of these structures will be broken, and the band structure of the lattice may also change to some extent. Using uniaxial strain, the noncentrosymmetric 2D unit cell will incur the relative displacement and generate a dipole moment based on the noncoincident centers of positive and negative charges. After the superposition of dipole moments, a macroscopic out-of-plane piezoelectricity will be created.

In this work, combined with the structural symmetry analysis and symmetry operations, the Janus monolayers of F-M-H (M = B, Al, and Ga) are theoretically simulated, first, by bridging the B-B bond of borophene through F (above) and H (below) atoms to form a honeycomb lattice structure. Al and Ga are in the same site of B, forming the other two

*wangxiaochun@jlu.edu.cn

structures. Since the H (above) atoms were replaced by F atoms, the Dirac cone of the *Cmmm* (B_4H_4) sheet was broken and it turned into a semiconductor material. Second, free imaginary frequency near the high-symmetry points and the slight potential energy fluctuation of each atom around a fixed value reveals the dynamic and thermal stabilities of the Janus F-*M*-H sheets. Moreover, the calculation results of Young's modulus and Poisson's ratio show that the three materials are flexible elastic piezoelectric materials. Additionally, the piezoelectric polarization of h-BN, 2H-MoS_2, and group-II oxides are usually limited to the in-plane direction [29,30]. On the contrary, the Janus monolayers of F-*M*-H are able to generate an ideal out-of-plane piezoelectric effect by applying the uniaxial strain along *z*-axis direction. In the case of relaxed ions, the coefficients e_{31}, e_{32}, and e_{33} are excellent. The lowest piezoelectric coefficient e_{31} among the three F-*M*-H monolayers is also much higher than those materials with out-of-plane piezoelectricity by up to two orders of magnitude, such as the group V-IV-III-VI film of SnN-InO ($e_{31} = 15.08 \times 10^{-10}$ C/m) and the Janus transition metal dichalcogenide of SnOSe ($e_{31} = 0.40 \times 10^{-10}$ C/m) [31,32]. Our results also reveal the relationship between the piezoelectric magnitude and the electronegativity difference ratio. Finally, the polarization changes linearly with the uniaxial strain, which can be enough to solve the problem that voltage cannot be measured precisely in the bionic skin sensors [33].

II. COMPUTATIONAL DETAILS

In this work, the Vienna *ab initio* simulation package (VASP) [34,35], the *ab initio* first-principles calculations based on density functional theory (DFT), the generalized gradient approximation (GGA) with the Perdew-Burke-Ernzerhof (PBE) [36,37], the projector augmented wave (PAW), and the plane wave basis were applied to complete the calculation [38]. The kinetic energy cutoff of the plane wave adopted was 530 eV. To avoid the interaction between adjacent layers due to the periodic structure, the vacuum layer of 18 Å was set. The first Brillouin zone of the honeycomb Janus F-*M*-H structures adopted a $5 \times 7 \times 1$ *k*-point grid for sampling [39]. For the relaxed structure, the forces of each atom in the primitive cell are lower than 10^{-4} eV/Å. The change of the total energy is lower than 10^{-6} eV. The effect of spin polarization is considered in the optimization, band structures, and piezoelectric calculations. The phonon spectrum was calculated by using density functional perturbation theory (DFPT) with a $25 \times 25 \times 1$ *k*-point grid to prove the dynamic stability [40]. The thermal stability of Janus F-*M*-H single-layers was also proved by executing the *ab initio* molecular dynamics (AIMD) simulations. Under the above setting, the piezoelectric coefficients e_{11} and d_{11} of BN were also calculated, and the obtained data ($e_{31} = 1.33 \times 10^{-10}$ C/m and $d_{11} = 0.59$ pm/V) were basically consistent with references ($e_{31} = 1.38 \times 10^{-10}$ C/m and $d_{11} = 0.60$ pm/V) [29].

III. RESULTS AND DISCUSSION

A. Optimum structure and material stability

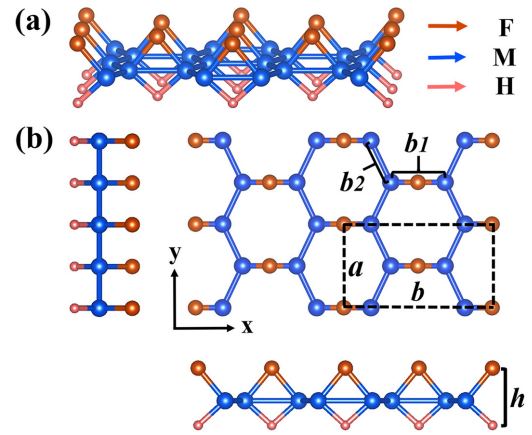After all the atoms' relaxation, the optimized unit cells of Janus F-*M*-H (*M* = B, Al, or Ga) are obtained. B, Al, and Ga

FIG. 1. (a) Bird's eye view and (b) top and side views of the F-*M*-H (*M* = B, Al, or Ga). Dashed-line box represents the cell.

atoms are sandwiched by F (above) and H (below) atoms, forming a F-*M*-H three-atom thickness layer. Top and side views of the Janus F-*M*-H single layer (2×2) are supported in Fig. 1. The b_1 stands for the distance of *M*-*M* that is bridged by F and H atoms, and the b_2 stands for an undecorated *M*-*M* bond. *a* and *b* are lattice parameters of the F-*M*-H 2D unit cells. *h* is the thickness of monolayers. The F-*M*-H structure is based on the structure with dynamical and thermal stability in Refs. [22,23]. In addition, the structure with the F atom located over the b_2 bond and H atom located under the b_1 bond is also tested. The optimized structure is distorted, and the total energy is higher than that of the structures with F and H atoms at the b_1 bond, which indicates the former is unstable. Therefore, this work only focuses on the structures with F and H atoms at the b_1 bond (shown in Fig. 1). The F-*M*-H crystal system belongs to the orthorhombic system, with space group of *Cmm*2. There are symmetry planes perpendicular to the *x* (armchair) or *y* (zigzag) directions, which means the F-*M*-H in-plane piezoelectric polarization is confined. F and H atoms break the symmetry with respect to the central *M* (*M* = B, Al, Ga) atoms, allowing a nonzero dipole moment existing along the direction of the *z* axis. Such case ensures that the polarization phenomenon appears along the *z* axis, which is vertical to the monolayer plane. In Table I, the b_2 bond length between the *M*-*M* atoms is on the order of $b_2(\text{Al}) > b_2(\text{Ga}) > b_2(\text{B})$, corresponding with the atomic radius order $R(\text{Al}) > R(\text{Ga}) > R(\text{B})$ [$R(\text{Al}) = 1.43$ Å, $R(\text{Ga}) = 1.22$ Å, and $R(\text{B}) = 0.80$ Å]. The b_1 bond length bridged with F and H atoms is longer than that without the element bridge. The different interaction strengths between *M*, F, and H atoms lead to the length order $b_1(\text{Ga}) > b_1(\text{Al}) > b_1(\text{B})$. The orthogonal primitive cell with four *M* atoms, two H atoms, and two F atoms is defined by lattice parameters *a*, *b*, and

TABLE I. Lattice constants of F-*M*-H primitive cells. The unit is Å.

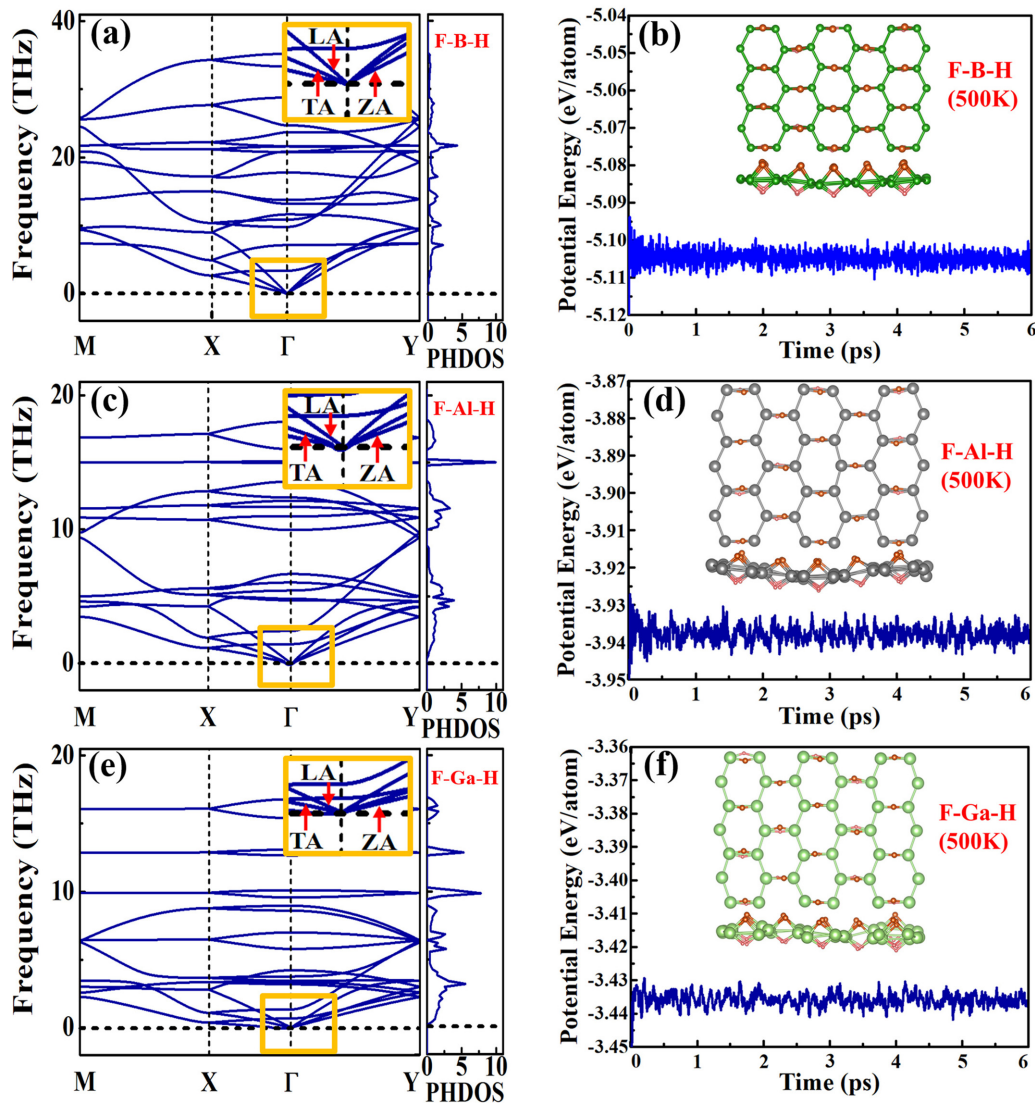| Material	a	b	h	b_1	b_2
F-B-H	5.51	3.11	2.14	2.01	1.72
F-Al-H	7.52	4.84	2.41	2.76	2.62
F-Ga-H	7.45	4.71	2.51	2.86	2.51

FIG. 2. (a), (c) and (e): The phonon spectra with corresponding phonon density of states (PHDOS). (b), (d) and (f): The *ab initio* molecular dynamics (AIMD) simulations of F-*M*-H sheets.

layer height *h*, which are marked by dashed lines and the solid line, respectively [Fig. 1(b)]. The lager the atomic radius of *M* atoms, the greater the lattice constants on the order of F-Al-H > F-Ga-H > F-B-H. Considering the interaction between atoms, the order of the thickness *h* is *h*(F-Ga-H) > *h*(F-Al-H) > *h*(F-B-H) (2.51 Å > 2.41 Å > 2.14 Å).

To verify the dynamical stability of F-*M*-H sheets, the phonon dispersions were calculated (see Fig. 2). No marked imaginary frequencies appear, confirming the dynamical stability of the monolayers F-*M*-H. Intriguingly, F-*M*-H (*M* = B, Al, and Ga) monolayers reveal diverse acoustic branches, optical branches, and vibration frequencies. In a polyatomic system, for each polarization or mode of polarization in a given direction of propagation, the dispersion relationship of the frequency with respect to the wave vector will evolve into two branches—acoustic and optical branches. According to the principle of phonon dispersion, for an eight-atom primitive cell, there are twenty-four phonon dispersion branches, in which three of them are acoustic modes and the other twenty-one are optical modes. However, in order to check the

imaginary frequency near high-symmetry points, four phonon modes in the *M*-*X*-Γ-*Y* region were not drawn. Notably, three acoustic branches are gathered at the highly symmetric Γ point, two linearly dispersive acoustic modes (longitudinal in-plane acoustic mode LA and transverse in-plane acoustic mode TA) and a transverse out-of-plane acoustic branch ZA with the lowest frequency dispersion, which are the features of the layered materials [41,42]. The slopes of the acoustic modes supported on the left and right of the gamma point are different, reflecting the presence of plane anisotropy [43]. The high-frequency optical modes are contributed by light atoms, and the remaining low-frequency phonon modes are contributed by heavy atoms [23]. The phonon density of states (PH-DOS) on the right corresponds well to the corresponding phonon spectra. Additionally, the thermal stability of Janus monolayers is also proved by executing the *ab initio* molecular dynamics (AIMD) simulations. The $4 \times 4 \times 1$ supercells containing 64 atoms are free from oversize deformation. After the *NVT* ensemble simulations for 6 ps with a time step of 2 fs at 500 K, the potential energy for each atom has a slight

TABLE II. Clamped-ion and relaxed-ion elastic stiffness coefficient C_{ij}, Poisson's ratio ν, and Young's modulus Y of the F-M-H lattice structures. The units of C_{ij} and Y are N/m. Subscripts a and b represent the special directions of $\theta = 0°$ and $90°$, respectively.

Material	Clamped ion				Relaxed ion							
	C_{11}	C_{12}	C_{22}	C_{66}	C_{11}	C_{12}	C_{22}	C_{66}	ν_a	ν_b	Y_a	Y_b
F-B-H	109.90	12.17	124.78	44.74	100.35	15.22	115.38	38.09	0.13	0.15	98.34	113.07
F-Al-H	47.32	5.46	45.00	11.10	25.02	11.83	41.23	8.75	0.29	0.47	21.63	35.64
F-Ga-H	47.32	2.02	43.78	10.78	23.34	8.61	40.99	8.48	0.21	0.37	21.53	37.82

fluctuation around a fixed value, which shows that the F-M-H sheets are thermally stable. The matching computation results are plotted in Fig. 2. In addition, the formation energy of F-M-H was calculated according to the formula [32]

$$\Delta E = (E - n_1 \times E_1 - n_2 \times E_2 - n_3 \times E_3)/n, \quad (1)$$

where E is the energy of the F-M-H Janus monolayer. E_1, E_2, and E_3 represent the per atom crystal energy of F, M, and H in the solid phase, respectively. n_1, n_2, and n_3 show the number of each element in the unit cell. And n is the total number of atoms. The formation energies ΔE of F-B-H, F-Al-H, and F-Ga-H are -0.99 eV, -1.91 eV, and -1.20 eV, respectively. Commonly, a negative value means that the structure is thermodynamically stable. Furthermore, the formation energy of F-M-H (M = B, Al, and Ga) is lower than B$_4$H$_4$ (-0.84 eV), indicating that the formation of F-M-H is stable.

Next, to research the mechanical stability and capabilities of the F-M-H, we calculated the elastic stiffness coefficient, Poisson's ratio, and Young's modulus. According to the Born-Huang criteria [44], the elastic stiffness coefficients of F-M-H meet the conditions of $C_{11}C_{22} - C_{12}^2 > 0$ and $C_{66} > 0$, which show that the F-M-H monolayers have mechanical stability. The Poisson's ratio and Young's modulus are calculated by the formulas [45]

$$\nu(\theta) = \frac{C_{12}\cos^4\theta - B\cos^2\theta\sin^2\theta + C_{12}\sin^4\theta}{C_{22}\cos^4\theta + A\cos^2\theta\sin^2\theta + C_{11}\sin^4\theta}, \quad (2)$$

$$Y(\theta) = \frac{C_{11}C_{22} - C_{12}^2}{C_{22}\cos^4\theta + A\cos^2\theta\sin^2\theta + C_{11}\sin^4\theta}, \quad (3)$$

where $A = (C_{11}C_{22} - C_{12}^2)/C_{66} - 2C_{12}$ and $B = C_{11} + C_{22} - (C_{11}C_{22} - C_{12}^2)/C_{66}$; θ is the angle of the arbitrary direction with respect to the armchair axis (x axis). That is, the armchair direction is along the direction of $\theta = 0°$; the zigzag direction (y axis) is along the direction of $\theta = 90°$.

In Table II, "relaxed ion" indicates the total elastic stiffness coefficient when considering the contributions of the rigid ionic distortions and ionic relaxation. "Clamped ion" denotes the elastic stiffness coefficient when only the rigid ionic distortion is considered. The ionic distort means to proportionally move the ionic position without optimization. The ionic relaxation indicates to optimize the atomic positions and achieve the structure with lowest energy. Poisson's ratio ν and Young's modulus Y are calculated from the total elastic stiffness coefficient. Y_a and Y_b represent the Young's modulus with the angle (θ) $0°$ and $90°$, respectively; ν_a, ν_b are the Poisson's ratio with the angle (θ) $0°$ and $90°$, respectively. In the calculation formulas of Poisson's ratio and Young's modulus [Eqs. (2) and (3)], the numerator of the former is

more complicated than that of the later. Then there is not certain relation between the Poisson's ratio and Young's modulus. The Young's modulus difference between Al and Ga is small, but this small difference is magnified at Poisson's ratio. The results show that the F-M-H monolayers are much softer than graphene (with elastic stiffness value of 330 N/m) [46]. Sn-based monolayers, such as the SnO$_2$ monolayer, are materials with the mechanically flexible nature [32]. The Y_a of F-M-H sheets are smaller than the Young's modulus of SnO$_2$ by 26.96, 103.67, and 103.77 N/m. The Poisson's ratio ν_b of F-Al-H and F-Ga-H is higher than that of SnO$_2$ by 0.23 and 0.13, respectively. In the clamped ion, the elastic stiffness coefficient C_{11} of F-Al-H and F-Ga-H is 47.31664 and 47.32065 N/m, respectively. Keeping two significant digits after the decimal point, the value of both C_{11} is 47.32 N/m. The elastic stiffness coefficients of F-B-H are larger as compared to F-Al-H and F-Ga-H, suggesting that the F-B-H sheet is even stiffer for curling due to the strong in-plane B-B bond. For F-B-H, Fig. 3 shows that the elastic stiffness coefficients along b_1 ($\theta = 0°$) and b_2 ($\theta = 115°$) are approximately equal. However, the elastic stiffness coefficients along b_1 ($\theta = 0°$) are smaller than that along b_2 ($\theta = 112°$ or $110°$) for the F-Al-H or F-Ga-H monolayer. This indicates that bridged elements may make the material softer. All the Y_a of the three materials are smaller than Y_b, indicating the x direction is easier to be deformed. In the whole range of angles, the elastic stiffness coefficients of F-Al-H and F-Ga-H are approximately equal; see Fig. 3(a). The values of Poisson's ratios ν_a and ν_b of the F-B-H ($\nu_a = 0.13$ and $\nu_b = 0.15$) are significantly smaller than those of F-Al-H ($\nu_a = 0.29$ and $\nu_b = 0.47$) and F-Ga-H ($\nu_a = 0.21$ and $\nu_b = 0.37$), which indicates F-B-H is harder to show transverse deformation while being applied
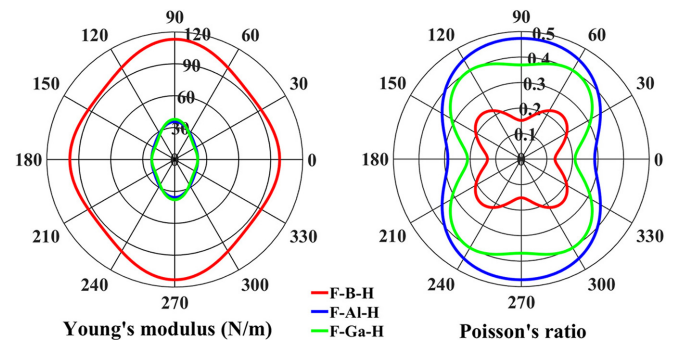

FIG. 3. The angle dependence relations of Young's modulus and Poisson's ratio. The figures of the periphery represent the θ angle (from $0°$ to $360°$), and the numbers in the vertical direction represent the values of Young's modulus and Poisson's ratio.
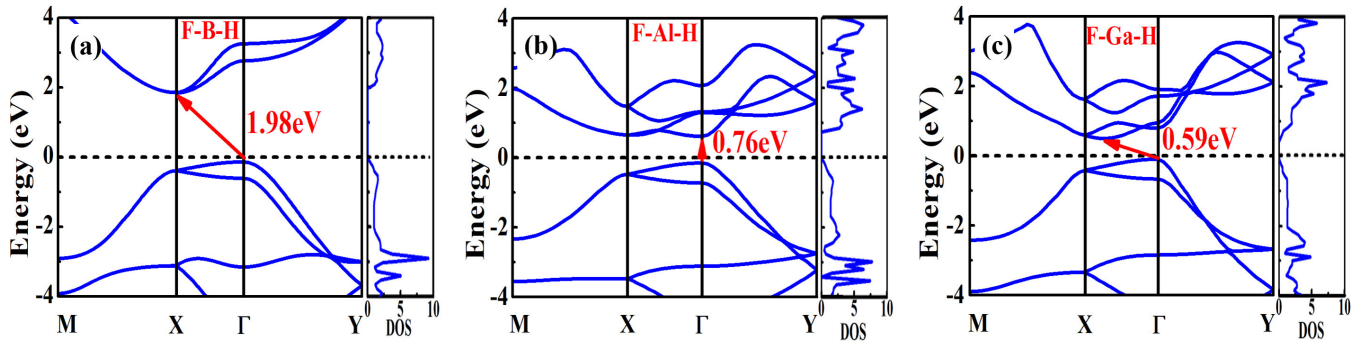
FIG. 4. The bands with the corresponding density of states (DOS) of F-*M*-H monolayers. The unit of DOS is states/(eV · unit cell). The Fermi level is set to zero. *M* (0.5, 0.5, 0), *X* (0.5, 0, 0), Γ (0, 0, 0), and *Y* (0, 0.5, 0) are symmetry points in the first Brillouin zone.

axial deformation than F-Al-H and F-Ga-H. The similar values of v_b and v_b for the F-B-H indicate that F-B-H has weaker mechanical anisotropy. The elastic stiffness coefficient and Poisson's ratio suggest that the Janus F-*M*-H sheets are decent elastic materials with commendable potentials for application in flexible devices.

B. Band structures

To analyze electronic properties of F-*M*-H, the band structures and the total density of states are calculated by using PBE method. Figure 4 shows that the three monolayers of F-*M*-H are semiconductors, which have no convergence of bands at the Fermi level. The valence band maximums (VBMs) are located at the Γ point (0.0, 0.0, 0.0), and the conduction band minimums (CBMs) appear at the *X* point (0.5, 0.00.0), Γ point (0.0, 0.0, 0.0), and *X*-Γ for F-B-H, F-Al-H, and F-Ga-H, respectively. Since the lowest point of the conduction band and the highest point of the valence band appear at different *K* points, F-B-H and F-Ga-H produce indirect band gaps. However, F-Al-H generates a direct band gap. The F-B-H has much larger band gap (1.98 eV) than F-Al-H (0.76 eV) and F-Ga-H (0.59 eV) by at least 2.6 times. B, Al, and Ga belong to the same main group, and the atomic number of B is smaller than that of Al and Ga. Unlike Al and Ga which are metal, B is a metalloid. The binding force of B to the peripheral electrons is greater than that of Al and Ga, so the outermost electrons of B need to overcome higher energy to become conduction band electrons. The electronic structure of the semiconductor can forbid the free charge transfer among the monolayer. It helps to maintain the polarized charge located at different surfaces of the monolayer, which is ready to provide the potential difference for external applications.

C. Bader charge analysis and charge density difference

In order visually and intuitively understand charge distribution and the bond between atoms, the Bader charge analysis and the charge density difference of the F-*M*-H structures are calculated. The charge density difference of the F-*M*-H is defined as the differences between the charge density of F-*M*-H sheets and the superposition of each atom charge density, i.e., $\Delta\rho(\vec{r}) = \rho(\text{F-}M\text{-H}) - \sum_\mu \rho_{\text{atom}}(\vec{r} - \vec{R}_\mu)$ [47]. In 3D charge density difference diagrams (Fig. 5), the upper part is the side view and the lower part is the top view. All of them were

below the isosurface level of 0.006 $e/\text{Å}^3$. F and H atoms both tend to gain electrons. B, Al, and Ga all tend to lose electrons. It is easy for F or H atoms to form ionic bonds with *M* atoms. Particularly, the B-B bond is filled with the yellow isosurface, indicating that the bond b_2 is the strong covalent bond. The positive and negative values indicate the number of electrons lost and gained after Bader charge analysis [see Figs. 5(a), 5(b) and 5(c)]. Al contributes more electrons to F and H atoms than B and Ga because the electronegativity of Al is the smallest among B, Al, and Ga. Then, the Al has more positive charge, and the F and H atoms in F-Al-H have more negative charge than that of F-B-H and F-Ga-H. According to the charge values, for the three materials, the positive charge center is located between the H and *M* atoms, and the negative charge center is located between the F and *M* atoms. These lead to polarization phenomenon along the *z* axis of the three monolayers. The positive and negative charge centers can be
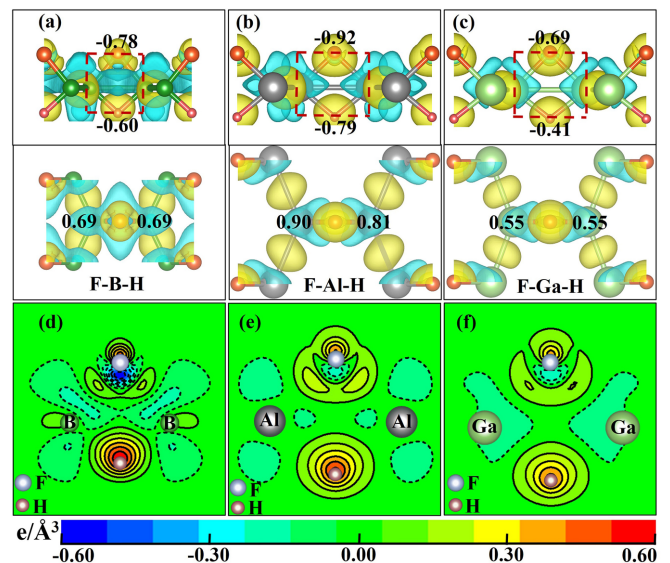

FIG. 5. The Bader charge analysis, and the 3D [(a), (b), and (c)] and 2D [(d), (e), and (f)] charge density difference of F-*M*-H. The red dotted box represents a two-dimensional cross section. The yellow and blue isosurfaces represent the accumulation and consumption of electrons, respectively. The color corresponding values in the two-dimensional differential charge density plots on the left can be viewed from the ruler on the right.

calculated by the formulas

$$\vec{R}(+) = \frac{\sum_{i=1}^{4} q_i^+ \, \vec{r}_i}{\sum_{i=1}^{4} q_i}, \tag{4}$$

$$\vec{R}(-) = \frac{\sum_{i=1}^{4} q_i^- \, \vec{r}_i}{\sum_{i=1}^{4} q_i}. \tag{5}$$

The subscript i indicates the number of atoms with positive or negative charges. q represents the Bader charge value. **r** is the position of each atom in F-M-H primitive cells. The total charges in the positive charge centers for the F-B-H, F-Al-H, and F-Ga-H are 2.76, 3.42, and 2.20 e/cell, respectively. Although the Al atom has the greatest amount of charge, the distance between the centers of positive and negative charges is an important factor affecting the value of the dipole moment, besides the charge value of the centers. Based on the theory of Bader charge analysis [48], most of the electronic charge located in the covalence band is divided and belongs to the neighboring atom's Bader charge. Then the Bader charge analysis can include the main electronic distribution for these systems, and can be used to deduce the location of the charge center. Figures 5(d), 5(e) and 5(f) are two-dimensional charge density difference maps (F, M, and H are coplanar; refer to the red dotted box for section drawing). The black solid line (the background is red and yellow) indicates the accumulation of charge ($\Delta\rho > 0$); the dashed line (the background is purple or blue) indicates the consumption of charges ($\Delta\rho < 0$).

To further study the polarization properties of materials, we also analyzed the F-M-H lattice materials from the perspective of electronegativity. The electronegativities of F, B, Al, Ga, and H atoms are 3.98, 2.04, 1.61, 1.81, and 2.20, respectively. The electronegativity of the M atom is smaller than F or H atoms on both sides of the monolayer, so M atoms will provide electrons to the upper and lower F or H atoms. The calculation shows that the ratio of electronegativity difference (r_{ed}) between M-F and M-H is 12, 6, and 4 for F-B-H, F-Ga-H, and F-Al-H, respectively. The electronegativity difference ratio can be calculated by the formula

$$r_{ed} = \frac{\mathrm{F}_{eln} - M_{eln}}{\mathrm{H}_{eln} - M_{eln}}, \tag{6}$$

where F_{eln}, M_{eln}, and H_{eln} represent electronegativity of F, M, and H atoms. In summary, the order of r_{ed} is $\mathrm{F} - \mathrm{B} - \mathrm{H} > \mathrm{F} - \mathrm{Ga} - \mathrm{H} > \mathrm{F} - \mathrm{Al} - \mathrm{H}$.

D. Piezoelectric coefficients

The linear part of the coupling effect between the dielectric and elastic properties of the crystal is the piezoelectric effect. Based on the analysis of the elastic stiffness coefficient and Poisson's ratio, the three F-M-H materials have flexible elastic property. In order to explore the piezoelectric properties of the material in detail, it is applied on the monolayers that the uniaxial strain is $\pm 0.5\%$ and $\pm 1\%$ along the x, y, and z directions, respectively. Applying pressure on the monolayer plane can realize the out-of-plane strain in the monolayer. In the experiment, when the monolayer is put into the liquid, the liquid will exert a pressure on the monolayer surface, which will lead to the out-of-plane strain in the monolayer. The

positive pressure and negative pressure of the liquid on the monolayer surface can approximately realize the compression and stretching along the out-of-plane direction. This method can be used to convert tidal energy and detect blood pressure. The piezoelectric strain tensor d_{ijk} and piezoelectric stress tensor e_{ijk} are described as follows [49]:

$$e_{ijk} = \partial P_i / \partial \varepsilon_{jk} = \partial \sigma_{jk} / \partial E_i, \tag{7}$$

$$d_{ijk} = \partial P_i / \partial \sigma_{jk} = \partial \varepsilon_{jk} / \partial E_i. \tag{8}$$

P_i, E_i, ε_{jk}, and σ_{jk} stand for the polarization, macroscopic electric field, stress tensor, and strain tensor. i, j, and k represent the x, y, and z directions, respectively. For simplicity, in the contracted Voigt notation, the third-order tensors d_{ijk} and e_{ijk} are usually expressed as d_{il} and e_{il}. The subscript i stands for x, y, or z axes, represented by the numbers 1, 2, and 3, respectively. l represents the second-order tensor xx, yy, zz, yz, zx, xy, which are represented by the numbers 1, 2, 3, 4, 5, and 6, respectively. d_{il} and e_{ik} are correlated by a fourth-order tensor elastic stiffness coefficient C_{kl}:

$$e_{il} = d_{ik} C_{kl}. \tag{9}$$

The determination of the piezoelectric coefficient and the elastic stiffness coefficient is inseparable from the symmetry of the monolayer. In the first section, it can be known that F-M-H belongs to the $Cmm2$ space group. There are two symmetry planes m_x and m_y that are respectively perpendicular to the x axis or y axis, and a secondary rotation axis along the z direction, which is noninverse symmetry. The initial elastic stiffness coefficient matrix is a 6×6 matrix. Considering the spatial symmetry of $Cmm2$, the matrix can be simplified as

$$C_{kl} = \begin{bmatrix} C_{11} & C_{12} & C_{13} & 0 & 0 & 0 \\ C_{12} & C_{22} & C_{23} & 0 & 0 & 0 \\ C_{13} & C_{23} & C_{33} & 0 & 0 & 0 \\ 0 & 0 & 0 & C_{44} & 0 & 0 \\ 0 & 0 & 0 & 0 & C_{55} & 0 \\ 0 & 0 & 0 & 0 & 0 & C_{66} \end{bmatrix}. \tag{10}$$

In the same way, the third-order piezoelectric strain tensor matrix is derived as

$$d_{ik} = \begin{bmatrix} 0 & 0 & 0 & 0 & d_{15} & 0 \\ 0 & 0 & 0 & d_{24} & 0 & 0 \\ d_{31} & d_{32} & d_{33} & 0 & 0 & 0 \end{bmatrix}. \tag{11}$$

The corner mark i of the piezoelectric strain coefficient represents the direction of polarization. According to the symmetry of three monolayers, there is no remaining polarization in the x or y direction, so $d_{24} = d_{15} = 0$. Considering the above factors, the expression of piezoelectric strain coefficient is obtained:

$$d_{31} = \frac{A e_{31} + B e_{32} + C e_{33}}{G}, \tag{12}$$

$$d_{32} = \frac{D e_{32} + E e_{33} + B e_{31}}{G}, \tag{13}$$

$$d_{33} = \frac{F e_{33} + C e_{31} + E e_{32}}{G}, \tag{14}$$

where $A = C_{22}C_{33} - C_{23}C_{23}$, $B = C_{23}C_{13} - C_{12}C_{33}$, $C = C_{12}C_{23} - C_{13}C_{22}$, $D = C_{33}C_{11} - C_{13}C_{13}$, $E =$
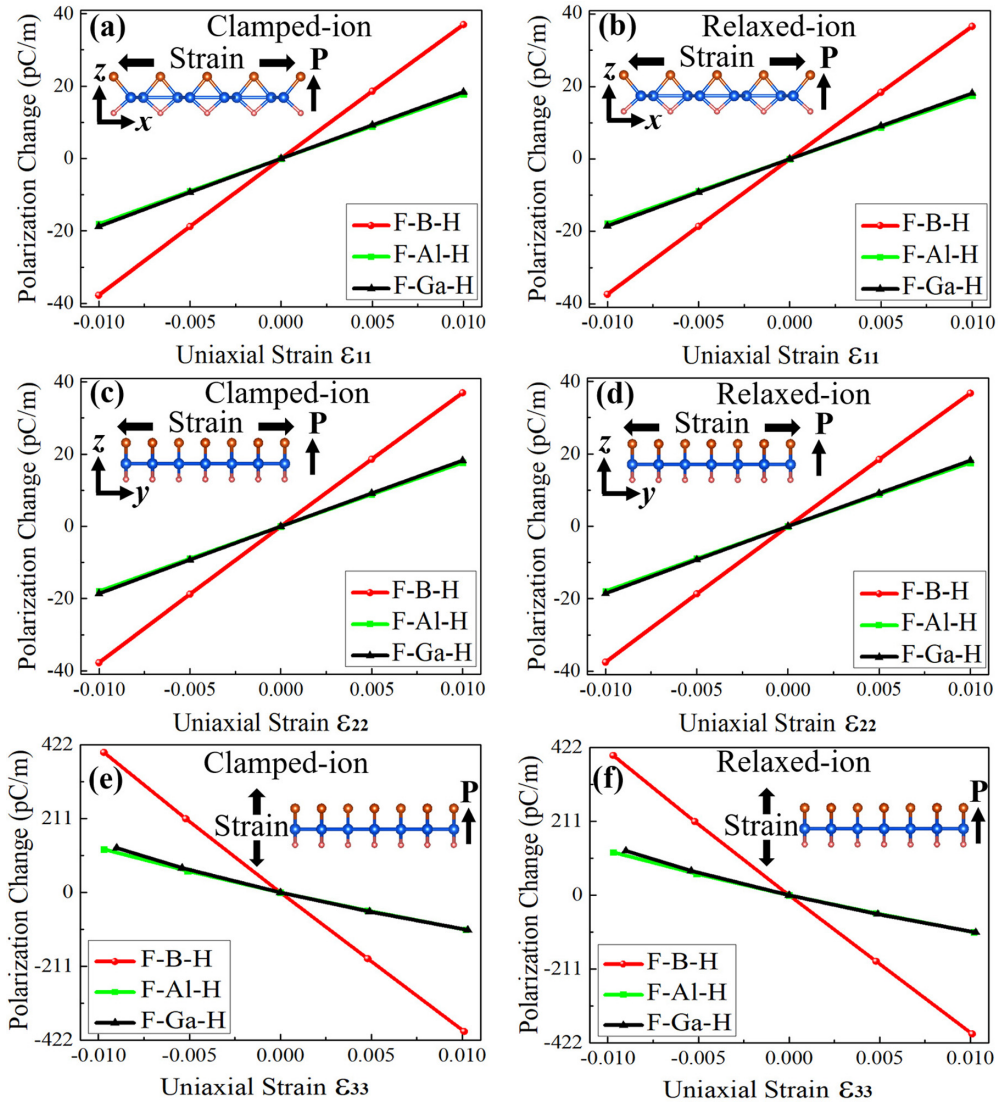
FIG. 6. Clamped-ion and relaxed-ion polarization change with the uniaxial strain ε_{11}, ε_{22}, and ε_{33}, respectively. The slopes of the lines represent the piezoelectric stress coefficients e_{31}, e_{32}, and e_{33}. **P** represents the direction of polarization.

$C_{13}C_{12} - C_{23}C_{11}$, $F = C_{22}C_{11} - C_{12}C_{12}$, and $G = C_{22}(C_{11}C_{33} - C_{13}C_{13}) + C_{12}(C_{23}C_{13} - C_{12}C_{33}) + C_{23}(C_{13}C_{12} - C_{11}C_{23})$.

Figures 6(a) and 6(b) illustrate the change of polarization with the uniaxial strain ε_{11}, where the slope of the line represents the piezoelectric coefficient e_{31}. For Figs. 6(c)–6(f), the piezoelectric coefficient e_{32} and e_{33} can be calculated based on the similar operation process. Considering Eqs. (12), (13), and (14), the piezoelectric strain coefficients d_{31}, d_{32}, and d_{33} can be obtained. The results are shown in Table III.

The total elastic stiffness coefficients are $C_{13} = -0.18$ N/m, $C_{23} = -0.23$ N/m, and $C_{33} = -5.46$ N/m of F-B-H; $C_{13} = -1.07$ N/m, $C_{23} = -0.58$ N/m, and $C_{33} = -3.91$ N/m of F-Al-H; and $C_{13} = 0.14$ N/m, $C_{23} = 0.52$ N/m, and $C_{33} = -2.59$ N/m of F-Ga-H. Whether in the clamped-ion or relaxed-ion situation, for the same monolayer, the piezoelectric stress coefficients e_{31} and e_{32} are very close. This is due to the similarity of symmetry operations in the x or y axis. It can be seen from Fig. 6 that the piezoelectric coefficient curves of F-Al-H

TABLE III. The piezoelectric stress coefficients e_{il} (in units of 10^{-10} C/m) and piezoelectric strain constants d_{ik} (in units of 10^{-10} m/V).

Material	Clamped ion						Relaxed ion					
	e_{31}	e_{32}	e_{33}	d_{31}	d_{32}	d_{33}	e_{31}	e_{32}	e_{33}	d_{31}	d_{32}	d_{33}
F-B-H	37.38	37.38	−401.62	0.44	0.41	73.55	37.00	37.13	−400.78	0.44	0.41	73.40
F-Al-H	17.93	17.79	−115.10	1.80	0.32	28.89	17.68	17.73	−114.52	1.79	0.32	28.74
F-Ga-H	18.58	18.43	−120.69	0.62	−0.27	46.53	18.33	18.35	−120.07	0.61	−0.26	46.29

and F-Ga-H are closely adjacent. Al and Ga are adjacent elements in the same main group and have similar peripheral electron distribution and metal character. In contrast, B is a metalloid. These facts lead to similar piezoelectricity of F-Al-H and F-Ga-H, which is different from F-B-H. Notably, the piezoelectric stress coefficient of F-B-H is greater than F-Ga-H and F-Al-H. Excitingly, the lowest coefficient e_{31} of F-Al-H is also much higher than those materials with out-of-plane piezoelectric effect, such as AlAs ($e_{31} = 0.40 \times 10^{-10}$ C/m) [50], the SnN-InO sheet ($e_{31} = 15.08 \times 10^{-10}$ C/m) [31], and recently reported 2D piezoelectric materials MoSO ($e_{31} = 1.40 \times 10^{-10}$ C/m) [51], the 2H VSSe monolayer ($e_{31} = 0.95 \times 10^{-10}$ C/m) [52], and SnOSe ($e_{31} = 0.40 \times 10^{-10}$ C/m) [32] in the relaxed-ion condition. The piezoelectric strain coefficients d_{31} of F-M-H (0.44×10^{-10} m/V, 1.79×10^{-10} m/V, and 0.61×10^{-10} m/V) are larger than the Janus monolayers of H-PG-F ($d_{31} = 0.69 \times 10^{-12}$ m/V) [3] and SnOSe ($d_{31} = 0.50 \times 10^{-12}$ m/V) [32]. The values of e_{33} are an order of magnitude higher than e_{3i} ($i = 1, 2$) and the coefficient of d_{33} are one to two orders of magnitude higher than d_{3i} ($i = 1, 2$), which show that a stronger piezoelectric effect exists by using uniaxial strain in the z-axis direction. The ratios of the electronegativity difference between M-F and M-H are 12, 6, and 4 in F-B-H, F-Ga-H, and F-Al-H, respectively. The order of piezoelectric stress coefficients is F-B-H > F-Ga-H > F-Al-H, which is consistent with the order of the ratio of electronegativity difference. We found a very interesting relationship: the higher the electronegativity difference ratio, the higher the piezoelectric stress coefficient, among these three monolayers. Electronegativity is a simply operable, qualitative, and rough criterion for considering the relationship with the piezoelectric coefficient. The different bonding condition of the B, Al, or Ga atom with the nearby atoms will also affect the electronic distribution around the B, Al, or Ga atom beside the effect of electronegativity. This will also contribute the piezoelectric performance of these monolayers in some degree. In the left panels of Fig. 7, the black axis on the left represents the distance between F and H atoms. The direction vector is not considered here, and the purple axis on the right represents the average of the Bader charges' absolute value carried by the positive and negative charge centers. The insets in the left panels represent that the vertical distance L (between the positive and negative charge centers) changes with the uniaxial strain ε_{33} increasing. With the increase of uniaxial strain ε_{33}, the Bader charge value of the F atom gradually decreases, but the z value of the F atomic position gradually increases. The Bader charge value of the H atom gradually increases, but the z value of the H atomic position gradually decreases. The Bader charge value and atomic position of the M ($M =$ B, Al, Ga) atom basically remain unchanged, which makes that the vertical distance L between positive and negative charge centers changes insignificantly. The positions of positive and negative charge centers are calculated based on Eqs. (4) and (5). As shown in the insets of the left panels of Fig. 7, L remains constant or increases slightly. However, with the increase of strain, the left panels show that the distance between the F and H atoms is also increased. It indicates that the interaction between atoms decreases, which leads to the decrease in the total number

of electrons obtained by H and F atoms and the decrease in the total number of electrons lost by middle-layer atoms. This results in the decrease in the average of the charges' absolute value carried by the positive and negative charge centers. In the right panels of Fig. 7, the blue axis on the left represents the total dipole moment of electrons and ions, and the red axis on the right represents the corresponding bottom area S of the unit cell under different strains. The polarization intensity is determined by the dipole moment and the bottom area. The absolute value of dipole moment is greatly affected by Bader charge and will show a decreasing trend, which is consistent with the Bader charge change trend in the left panels. It should be noted that the Bader charge is only a qualitative auxiliary and operable method to analyze the distribution of polarization charge. The dipole moment is determined by the contributions of electrons and ions. In the right panels of Fig. 7, the bottom area of the unit cell also decreased gradually, and the decreasing percentages are 19.36%, 12.17%, and 12.00%. The percentages of dipole moment absolute value decrease are 0.08%, 0.06%, and 0.05%, respectively. With the increase of uniaxial strain ε_{33}, the bottom area decline trend is more obvious than the decline trend of dipole moment absolute value. So the absolute value of polarization intensity shows a gradual increasing trend for the F-M-H. This is consistent with data as mentioned above. In Fig. 6(f), the absolute values of polarization intensity are also increasing under the uniaxial strain, while each of the polarization intensities is negative. The bottom area S decrease proportion of F-B-H is significantly larger than F-Al-H and F-Ga-H. So the F-B-H finally shows a stronger piezoelectric property. The above analysis is also applicable to the case for uniaxial strain ε_{11} or ε_{22}.

The atomic and electronic structure of the F-M-H is asymmetric along the z direction. The asymmetry of the electronegativity of the atoms along the z axis introduces the asymmetric distribution of the Bader charge in F-M-H. These facts lead to the F-M-H possessing the strong polarization property along the z axis. This extremely large piezoelectric effect by applying uniaxial strain on the z axis makes the Janus F-M-H a remarkable, novel, and promising sheet piezoelectric material. It also can provide electrons for other 2D coating material so that it ultimately accelerates the occurrence of chemical reactions catalyzed by the coating material. We expect that the remarkable vertical linear piezoelectric polarization of the F-M-H Janus monolayer can provide new opportunities for the design of piezoelectric devices.

IV. CONCLUSION

In summary, the F-M-H ($M =$ B, Al, and Ga) monolayers are predicted based on B_4H_4 2D nanostructure and prove to have remarkable vertical piezoelectricity by employing uniaxial strain in the z-axis direction. The F-M-H structures are dynamically and thermally stable based on the DFPT and AIMD simulations. The band structures show that all three F-M-H materials are semiconductors, which meets the requirement of piezoelectric property. The mechanical stability and the elastic capabilities of F-M-H monolayers indicate that they can be effectively and tautologically applied in flexible piezoelectric devices. The piezoelectric stress coefficient of
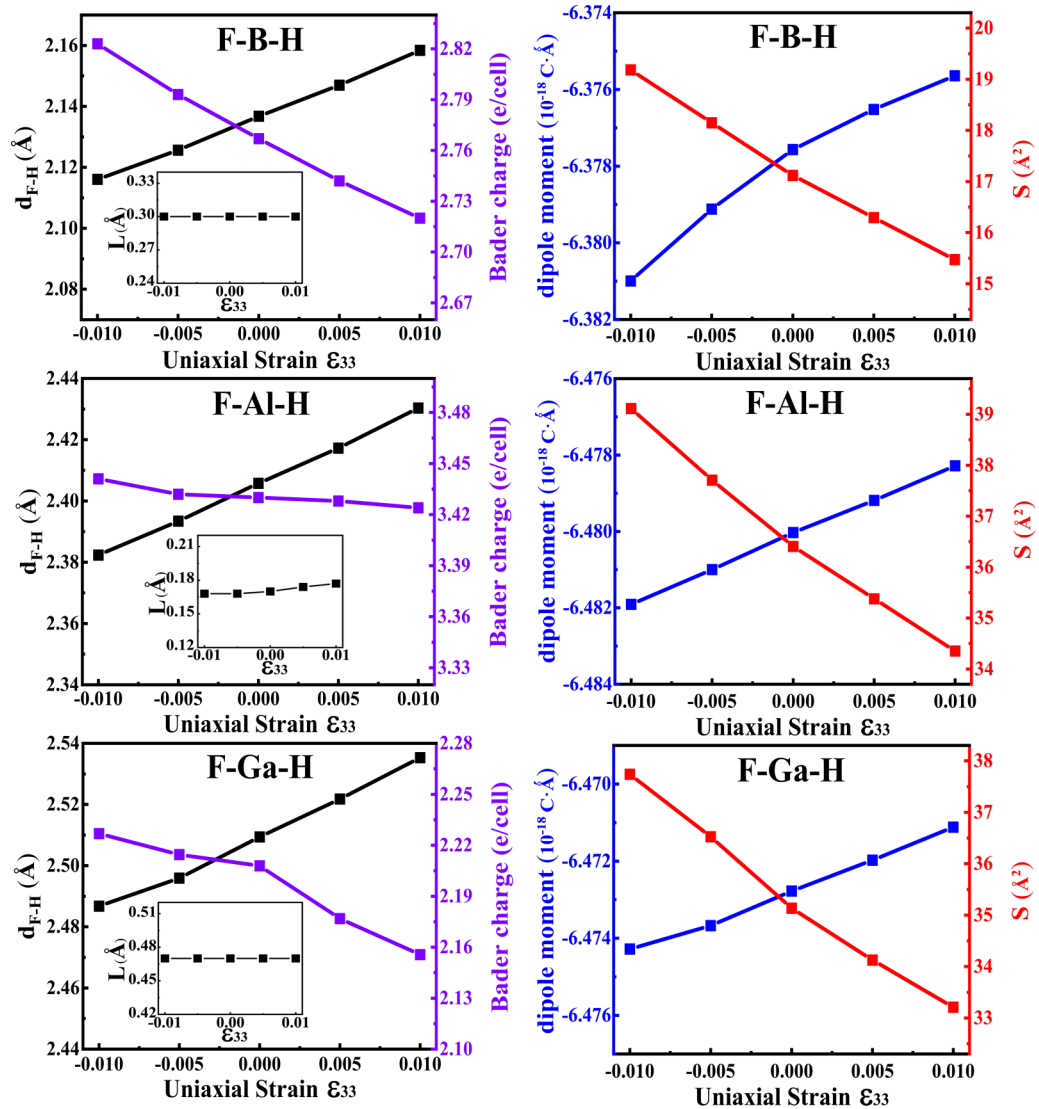
FIG. 7. Left panels: The relationship of the distance between F and H atoms and the average of the Bader charge absolute value carried by positive and negative charge centers with the uniaxial strain ε_{33}. The insets in the left panels show the vertical distance L (between the positive and negative charge centers) changes with the ε_{33} increasing. Right panels: The relationship of the total dipole moment and the bottom area S with the uniaxial strain ε_{33}.

F-B-H is greater than F-Ga-H and F-Al-H. For the three F-M-H monolayers, the increasing order of piezoelectric stress coefficients is consistent with the increasing order of the ratio of electronegativity difference. Excitingly, the polarization change is linear with the uniaxial strain, which can accurately measure piezoelectric values. The stable and flexible F-B-H monolayer with outstanding vertical piezoelectric coefficients e_{33} and d_{33} can further improve the practical applications of

wearable electronic blood pressure detectors and the robotic tactile sensors. The method can also inspire new solutions for the design of piezoelectric catalytic material.

[1] L.-L. Liu, C.-P. Chen, L.-S. Zhao, Y. Wang, and X.-C. Wang, Carbon **115**, 773 (2017).

[2] L.-S. Zhao, Y. Wang, C.-P. Chen, L.-L. Liu, H.-X. Yu, Y. Zhang, Y. Chen, and X.-C. Wang, Phys. E (Amsterdam) **91**, 82 (2017).

[3] H. J. Jia, H. M. Mu, J. P. Li, Y. Z. Zhao, Y. X. Wu, and X. C. Wang, Phys. Chem. Chem. Phys. **20**, 26288 (2018).

[4] L.-L. Liu, Y. Wang, C.-P. Chen, H.-X. Yu, L.-S. Zhao, and X.-C. Wang, RSC Adv. **7**, 40200 (2017).

[5] H.-Y. Yu, X.-C. Wang, and S. X.-A. Zhang, Appl. Surf. Sci. **563**, 150328 (2021).

[6] Y.-Z. Zhao, H.-J. Jia, S.-N. Zhao, Y.-B. Wang, H.-Y. Li, Z.-L. Zhao, Y.-X. Wu, and X.-C. Wang, Phys. E (Amsterdam) **117**, 113817 (2020).

[7] J.-P. Li, H.-J. Jia, D.-R. Zhu, X.-C. Wang, F.-C. Liu, and Y.-J. Yang, Appl. Surf. Sci. **463**, 918 (2019).

[8] H. Zhang, ACS Nano **9**, 9451 (2015).

[9] G. Zhu, R. Yang, S. Wang, and Z. L. Wang, Nano Lett. **10**, 3151 (2010).

[10] Z. Yu, Z.-Y. Ong, Y. Pan, Y. Cui, R. Xin, Y. Shi, B. Wang, Y. Wu, T. Chen, Y.-W. Zhang, G. Zhang, and X. Wang, Adv Mater. **28**, 547 (2016).

[11] X. L. Zhu, H. Yang, W. X. Zhou, B. Wang, N. Xu, and G. Xie, ACS Appl. Mater. Interfaces **12**, 36102 (2020).

[12] S. M. Nakhmanson, M. Buongiorno Nardelli, and J. Bernholc, Phys. Rev. Lett. **92**, 115504 (2004).

[13] H. Wu, P. Ren, P. Zhao, Z. Gong, X. Wen, Y. Cui, Q. Fu, and X. Bao, Nano Res. **12**, 85 (2018).

[14] I. Cabria and J. W. Mintmire, Europhys. Lett. **65**, 82 (2004).

[15] W. Ma, J. Lu, B. Wan, D. Peng, Q. Xu, G. Hu, Y. Peng, C. Pan, and Z. L. Wang, Adv. Mater. **32**, 1905795 (2020).

[16] L. C. Xu, A. Du, and L. Kou, Phys. Chem. Chem. Phys. **18**, 27284 (2016).

[17] B. Feng, J. Zhang, Q. Zhong, W. Li, S. Li, H. Li, P. Cheng, S. Meng, L. Chen, and K. Wu, Nat. Chem. **8**, 563 (2016).

[18] A. Lherbier, A. R. Botello-Méndez, and J.-C. Charlier, 2D Mater. **3**, 045006 (2016).

[19] A. J. Mannix, Z. Zhang, N. P. Guisinger, B. I. Yakobson, and M. C. Hersam, Nat. Nanotechnol. **13**, 444 (2018).

[20] N. R. Glavin, R. Rao, V. Varshney, E. Bianco, A. Apte, A. Roy, E. Ringe, and P. M. Ajayan, Adv. Mater. **32**, 1904302 (2020).

[21] Y. Jiao, F. Ma, J. Gu, Z. Chen, and A. Du, Nanoscale **12**, 10543 (2020).

[22] Y. Jiao, F. Ma, J. Bell, A. Bilic, and A. Du, Angew. Chem. Int. Ed. Engl. **55**, 10292 (2016).

[23] J. He, D. Li, Y. Ying, C. Feng, J. He, C. Zhong, H. Zhou, P. Zhou, and G. Zhang, npj Comput. Mater. **5**, 47 (2019).

[24] B. Lei, Y.-Y. Zhang, and S.-X. Du, Chin. Phys. B **28**, 046803 (2019).

[25] M. Shahrokhi, Comput. Mater. Sci. **156**, 56 (2019).

[26] M. Makaremi, B. Mortazavi, and C. V. Singh, Mater. Today Energy **8**, 22 (2018).

[27] V. Shukla, R. B. Araujo, N. K. Jena, and R. Ahuja, Phys. Chem. Chem. Phys. **20**, 22008 (2018).

[28] D. Li, J. He, G. Ding, Q. Q. Tang, Y. Ying, J. He, C. Zhong, Y. Liu, C. Feng, Q. Sun, H. Zhou, P. Zhou, and G. Zhang, Adv. Funct. Mater. **28**, 1801685 (2018).

[29] K.-A. N. Duerloo, M. T. Ong, and E. J. Reed, J. Phys. Chem. Lett. **3**, 2871 (2012).

[30] H. L. Zhuang, M. D. Johannes, M. N. Blonsky, and R. G. Hennig, Appl. Phys. Lett. **104**, 022116 (2014).

[31] D.-R. Zhu, Y. Wu, H.-N. Zhang, L.-H. Zhu, S.-N. Zhao, and X.-C. Wang, Phys. E (Amsterdam) **124**, 114214 (2020).

[32] X. Zhang, Y. Cui, L. Sun, M. Li, J. Du, and Y. Huang, J. Mater. Chem. C **7**, 13203 (2019).

[33] H. Chen, L. Miao, Z. Su, Y. Song, M. Han, X. Chen, X. Cheng, D. Chen, and H. Zhang, Nano Energy **40**, 65 (2017).

[34] G. Kresse and J. Hafner, Phys. Rev. B **48**, 13115 (1993).

[35] J. Paier, M. Marsman, K. Hummer, G. Kresse, I. C. Gerber, and J. G. Angyan, J. Chem. Phys. **124**, 154709 (2006).

[36] J. P. Perdew, J. A. Chevary, S. H. Vosko, K. A. Jackson, M. R. Pederson, D. J. Singh, and C. Fiolhais, Phys. Rev. B **46**, 6671 (1992).

[37] A. D. Becke, Phys. Rev. A **38**, 3098 (1988).

[38] P. E. Blochl, Phys. Rev. B **50**, 17953 (1994).

[39] H. J. Monkhorst and J. D. Pack, Phys. Rev. B **13**, 5188 (1976).

[40] L.-F. Huang, P.-L. Gong, and Z. Zeng, Phys. Rev. B **91**, 205433 (2015).

[41] J. W. Jiang, B. S. Wang, J. S. Wang, and H. S. Park, J. Phys.: Condens. Matter **27**, 083001 (2015).

[42] H. Soni and P. K. Jha, AIP Adv. **5**, 107103 (2015).

[43] C. Zhong, W. Wu, J. He, G. Ding, Y. Liu, D. Li, S. A. Yang, and G. Zhang, Nanoscale **11**, 2468 (2019).

[44] J. Wang, S. Yip, S. R. Phillpot, and D. Wolf, Phys. Rev. Lett. **71**, 4182 (1993).

[45] M. Yagmurcukardes, C. Sevik, and F. M. Peeters, Phys. Rev. B **100**, 045415 (2019).

[46] M. Yagmurcukardes, R. T. Senger, F. M. Peeters, and H. Sahin, Phys. Rev. B **94**, 245407 (2016).

[47] X. Wang, Q. Lin, R. Li, and Z. Zhu, Phys. Rev. B **73**, 245404 (2006).

[48] M. Yu and D. R. Trinkle, J. Chem. Phys. **134**, 064111 (2011).

[49] L. Dong, J. Lou, and V. B. Shenoy, ACS Nano **11**, 8242 (2017).

[50] M. N. Blonsky, H. L. Zhuang, A. K. Singh, and R. G. Hennig, ACS Nano **9**, 9885 (2015).

[51] M. Yagmurcukardes and F. M. Peeters, Phys. Rev. B **101**, 155205 (2020).

[52] C. Zhang, Y. Nie, S. Sanvito, and A. Du, Nano Lett. **19**, 1366 (2019).